Zhu, M., Zhang, S. Y., Jiang, J. Z., Macdonald, J. H. G., Neild, S. A., Antunes, P., Pombo, J., Cullingford, S., Askill, M., & Fielder, S. (2021). Enhancing pantograph-catenary dynamic performance using an inertance-integrated damping system. *Vehicle System Dynamics: International Journal of Vehicle Mechanics and Mobility*. https://doi.org/10.1080/00423114.2021.1884273

Enhancing Pantograph-Catenary Dynamic Performance Using an Inertance-integrated Damping System

Ming Zhu[a], Sara Ying Zhang[b], Jason Zheng Jiang[a], John Macdonald[a], Simon Neild[a], Pedro Antunes[c,d], João Pombo[c,d,e], Stephen Cullingford[f], Matthew Askill[f], Stephen Fielder[f]

[a]Faculty of Engineering, University of Bristol, Bristol, UK; [b]Institute of Urban Smart Transportation and Safety Maintenance, Shenzhen University, Shenzhen, People's Republic of China; [c]Institute of Railway Research, University of Huddersfield, Huddersfield, UK; [d]IDMEC, Instituto Superior Técnico, Universidade de Lisboa, Lisbon, Portugal; [e]ISEL, Instituto Politécnico de Lisboa, Lisbon, Portugal; [f]Brecknell, Willis and Company Limited, Chard, Somerset, UK.

Corresponding author: Dr Jason Zheng Jiang (z.jiang@bristol.ac.uk)

Co-corresponding author: Dr Sara Ying Zhang (sara.zhangying@outlook.com)

[Word Count:6400 (approx.).]

Enhancing Pantograph-Catenary Dynamic Performance Using an Inertance-integrated Damping System

Abstract

For modern electrical rail systems, the pantograph-catenary dynamic performance is one of the most critical challenges. Too much fluctuation in contact forces leads to either accelerated wear of the contacting components or losses of contact and, consequently, arcing. In this work, inertance-integrated pantograph damping systems are investigated with the objective of reducing the contact force standard deviation. Firstly, a multibody pantograph model is developed with its accuracy compared with experimental data. The model is improved through the calibration of the pantograph head suspension parameters and the introduction of both non-ideal joint and flexibility effects. Using the calibrated model, beneficial inertance-integrated damping systems are identified for the pantograph suspension. The results show that the configuration with one inerter provides the best performance among other candidate layouts and contends a 40% reduction of the maximum standard deviation of the contact force over the whole operating speed range in the numerical modelling scenario analysed. Considering the identified configuration, time-domain analysis and modal analysis are investigated. It has been shown that the achieved improvement is due to the fact that with the beneficial inertance-integrated damping system, the first resonance frequency of the pantograph system coincides with the natural frequency of the catenary system.

Keywords: Pantograph-Catenary System, Dynamic Performance, Inerter, Multibody Dynamics, Damping System Design

Subject classification codes:

1. Introduction

High-speed trains are becoming one of the most sought after transportation modes due to their high travelling speed, reliability, convenience and low carbon emissions. Modern high-speed trains are driven by electricity transmitted from the catenary, which is generally achieved by the contact between the power receiving device, the pantograph, and the contact wires of the catenary. The pantograph-catenary system is the most practical and economic way to electrically power high-speed trains. However, it depends on reliable contact between the pantograph head and the contact wire. According to statistics consolidated over Europe, an average of over one million minutes of delay each year are linked to problems with the pantograph-catenary interface [1]. Reliable power transmission is one of the key challenges in ensuring efficient operation and one of the most critical factors that restrict the maximum

commercial operating speed of high-speed trains [2]. As operating speed increases, the vibrations of the pantograph-catenary system generally become stronger. Such vibrations deteriorate the power transmission, leading to contact losses with consequent arcing and accelerated wear of the contact components [3, 4]. Better pantograph-catenary contact dynamics is therefore critical for improving the transport operation efficiency and system reliability in the design of the next generation of trains and overhead system.

To study the pantograph-catenary interaction, Wu and Brennan [5] simplified the pantograph-catenary system as a time-varying single degree-of-freedom (DOF) lumped mass model and investigated the basic analytical dynamic performance. Pisano and Usai [6] used a simplified time-varying 1DOF lumped mass catenary model coupled with a 2DOF lumped mass pantograph model. Facchinetti *et al.* [7] developed a hardware-in-the-loop procedure based on a real-time catenary model to reproduce the realistic behaviour of the pantograph-catenary system. A fully three-dimensional interaction methodology is also developed based on the finite element method (FEM), for the catenary [8], and multibody dynamics methods, for the pantograph [9-11], integrated via an efficient co-simulation procedure [12, 13]. Other authors also devoted their attention to studying how pantograph-catenary performance is affected by service conditions such as contact wire irregularities [14-16], aerodynamic loads [17-19], wear [20, 21], multiple pantographs operations [22, 23] and track irregularities [24]. The effect of train excitations on the pantograph-catenary dynamics is also evaluated in the literature [25，26].

However, the focus of the above studies was mainly on the modelling and simulation, rather than dynamic performance optimisation. Park *et al*. [27] and Kim *et al*. [28] each investigated the parameter sensitivity of a FEM catenary coupled with a 3DOF lumped mass pantograph model and optimised the key design parameters. Zhou and Zhang [29] discussed the influence of the design parameters on the contact force and optimised the model parameters using a FEM catenary model coupled with a lumped mass pantograph model. Ambrósio *et al.* [10] also minimised the standard deviation of the contact force with a 3DOF lumped mass pantograph model. While these lumped mass models captured the behaviour well, the model parameters do not link conveniently to the physical characteristics of the pantograph. This means that, with this type of model, it is a challenge to know how the vibration suppression elements of the pantograph system might be altered to improve the overall system performance.

Separately, the inerter has been proposed as an element that can be used, alongside dampers and springs, to enhance the passive vibration suppression performance of systems. The inerter [30] is an ideal mechanical element with two terminals having the property that the generated force is proportional to the acceleration of its length. This completes the analogy between mechanical and electrical systems by providing the mechanical equivalence to a capacitor [31]. With the introduction of the inerter, all positive-real immittance functions can be realised by passive networks consisting of inerters, dampers and springs. Performance benefits from employing inerters have been identified for various mechanical systems, including motorcycle steering systems [32], passenger vehicle suspensions [33, 34], train suspensions [35-37], buildings [38-40], landing gear [41], wind turbines [42] and cables [43].

The main aim of the work presented in this article is to explore the potential benefits of extending the successful employment of inerters onto pantograph design. In this sense, a multibody pantograph model is developed with its accuracy enhanced based on existing literature. Consequently, the benefits of inertance-integrated damping systems on the dynamic performance of the pantograph-catenary system are investigated. This is done by considering various suppression system layouts using the structure-based method [44] applying to a multibody pantograph model. The standard deviation of the contact force, as one of the most important metrics of pantograph-catenary dynamics, is aimed to be reduced using the inertance-integrated damping configurations.

This paper is structured as follows. In Section 2, a multibody pantograph model is assessed against published experimental data with the limitations of the model discussed. In Section 3, the multibody model is further enhanced to better match the experimental data. Subsequently, in Section 4, beneficial inertance-integrated damping configurations are identified, with performance advantages presented and discussed. Conclusions and further developments are drawn in Section 5.

2. Development and assessment of a pantograph model

In this section, a simplified multibody pantograph model is developed with its accuracy compared with experimental data. Some discrepancies between the responses of the original model and the experimental data can be observed. The sources of the observed discrepancies are further discussed based on the mode shape analysis.

2.1. A multibody pantograph model and comparison with experimental data

A realistic 3D pantograph multibody model was developed by Ambrósio *et al*. [9, 17]. In [45], the parameters of this pantograph multibody model were optimised to fit its response better with the experimental data. Note that because this paper is a first conceptual study to investigate the benefits of the integrated-damping systems on pantographs and more advanced and detailed analyses will follow after the benefits are presented, a simplified pantograph model is considered in this work. It should also be noted that the main interest of this work is the contact forces between the pantograph and catenary, which occur in the vertical direction. Therefore, the 3D multibody model in the reference can be reduced to a 2D multibody model, which consists of 7 rigid bodies as shown in Figure 1, along with an actuator as used in the experiments [45]. In [9, 45], the local 3D coordinates are denoted as $[\xi_i, \eta_i, \zeta_i]$ where the subscript indicates the name of the body. In this work, the 2D coordinates, $[\xi_i, \zeta_i]$, which form the vertical plane, are abstracted from the original 3D coordinates in [9, 45] to establish the simplified multibody pantograph model here. The basic equations of motion of the model are explained in Appendix 1. All the parameter values of the original model are detailed in [9, 45]. In this work, rotation of the head is constrained and the head links to the stability arm by a prismatic joint which permits only vertical translational motion with respect to the top of the stability arm. The base suspension between point *b* and point *d*, modelled by spring k_1 and damper c_1 in parallel, and the head suspension between the head and the top of the stability arm, modelled by spring k_2 and damper c_2 in parallel, are applied in the pantograph system for vibration suppression, see Figure 1. A static actuator force $f_a = 10$ kN is applied between point *c* and point *d* to provide the uplift force to the pantograph, see Figure 1.

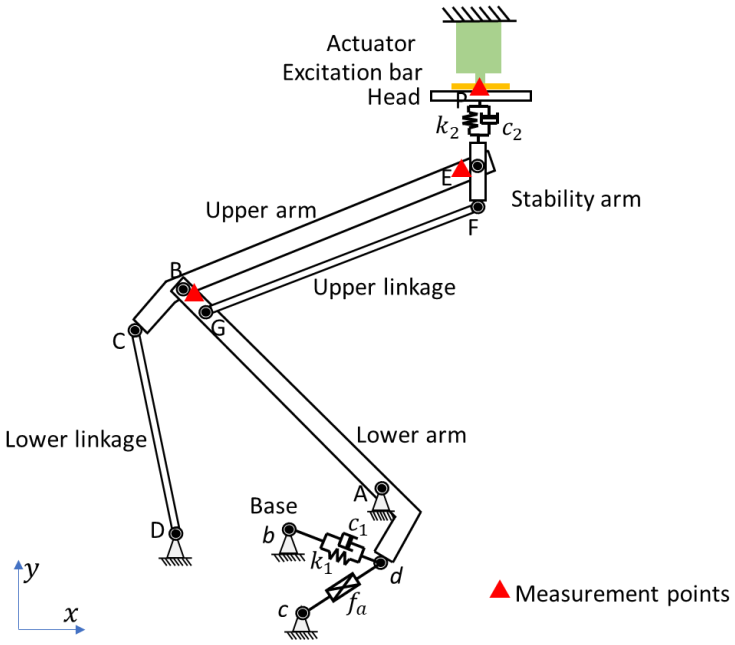

Figure 1. Diagram of the simplified multibody pantograph model, excitation and measurement points.

A series of physical dynamic tests of the pantograph have been carried out [7, 46]. A sequence of sinusoidal displacement excitations with 1 mm amplitude from 0 Hz to 20 Hz were applied on the head via the actuator shown in Figure 1. In [45], the frequency response functions (FRFs) of the measurement points are defined as

$$\mathrm{FRF}_i(f) = \frac{\mathrm{fft}(a_i(t), f)}{\mathrm{fft}(p_c(t), f)}, i \in \{P, E, B\}, f \in (0\ \mathrm{Hz}, 20\ \mathrm{Hz}] \quad (1)$$

where $a_i(t)$ and $p_c(t)$ are the vertical acceleration of the measurement point i (as shown in Figure 1, pantograph head, top of the upper arm, and top of the lower arm) and the contact force applied on the pantograph head at each individual excitation frequency f, respectively, and fft(·) is the Fourier transform at each corresponding individual excitation frequency f. The experimental FRF data is available in [45] and is shown as the solid lines in Figure 2. The same excitations have also been applied to the original numerical model in [9, 45], with the three FRF curves also included in Figure 2. Note that it has been checked that the developed 2D model has a very similar response compared with the original 3D model for all three measurement points. It is clear from Figure 2 that some discrepancies exist between simulation and experimental curves. Firstly, the frequencies of the first peaks (indicated with number 1) in the model are too low, while their amplitudes are too high, relative to the corresponding experimental peaks. Secondly, the amplitudes of the second peaks (indicated with number 2), are much higher for the original numerical model than for the experiments. Thirdly, there are peaks around 11 Hz (indicated with number 3) in the experimental data, which are not predicted using the original numerical model. There are also discrepancies in terms of the predicted phase when compared with the experimental data (Figure 2(b)). It is noted that the phases of the FRFs for the upper and lower arms are identical for the original model. This is because they belong to one linkage mechanism (formed by 4-bar mechanisms ABCD and BEFG, respectively, with BG in common), which hence share the same degree of freedom.

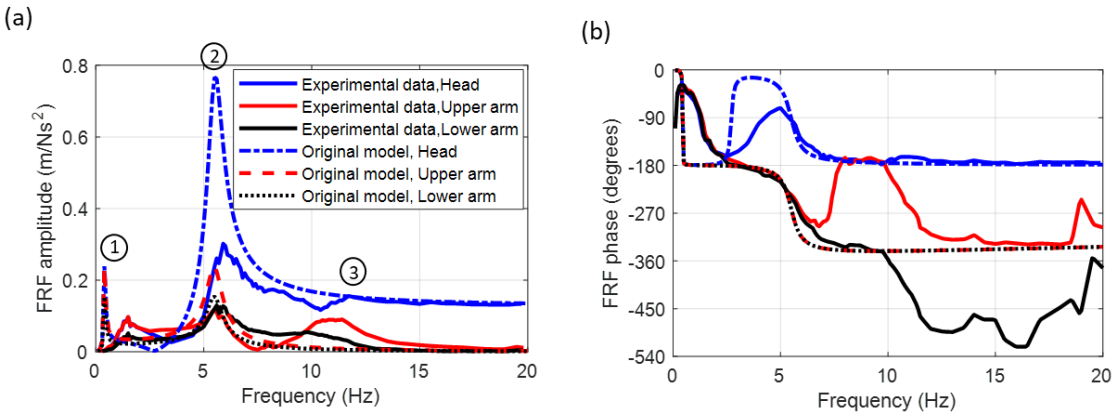

Figure 2. Comparison of the FRF, (a) amplitudes and (b) phases, between the original numerical multibody model and the experimental data taken from [45].

2.2. Analysis of the sources for the observed discrepancies

Basic mode shape analysis is considered here to find out the sources for the observed discrepancies. The original multibody model consists of 7 rigid bodies and has 2 DOFs in total. These are the head's relative vertical motion with respect to the top of the stability arm and the motion of the pantograph frame which is a mechanism with only 1 DOF. This explains why only two resonances are observed in the response spectra of the original numerical model (Figure 2). Considering the experimental FRFs, first resonance exhibits almost the same amplitudes of response for the head and top of the upper arm, with the lower arm response being about half of this, which is determined by the pantograph frame kinematics. Also, all three measurement points keep in-phase with each other in the frequency range of the first peak. These observations indicate that the first mode is dominated by pantograph frame mechanism motion with little contribution from the head. For the second peak of the experimental FRFs, the amplitudes of the top point of the upper arm and the lower arm are similar, while the amplitude of the head motion is significantly larger. For the phases, the head is almost in anti-phase with the other two measurement points. These observations of the second peak mean that this mode is dominated by the motion between the head and the top point of the upper arm. The mode shapes of the first two modes are sketched in Figure 3.

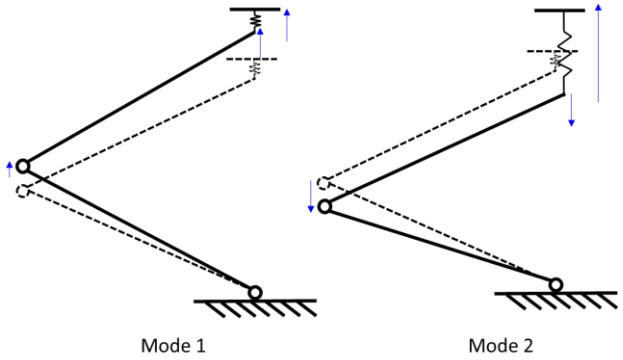

Figure 3. Sketches of the first two mode shapes of the pantograph.

The above mode shape analysis suggests that, for the original numerical multibody model, the reason why the frequencies of the first peaks are significantly lower while their amplitudes are higher than the corresponding experimental ones is that the stiffness and

damping of the pantograph frame mechanism are both underestimated. We hypothesise that this may be due to assuming that the arm joints are ideal, exhibiting no damping or stiffness [47]. Similarly, it is suggested that the higher amplitudes of the original numerical model's second peaks compared with the experimental ones, especially for the pantograph head, are because the damping of the head suspension is underestimated. In addition to the first two rigid body modes in the experimental FRFs, there are additional peaks around 11 Hz. This indicates that an additional DOF is needed in the numerical model, which could arise from a flexibility effect [11]. The phase gap of around 180 degrees, *i.e.*, anti-phase, between the top of the upper arm and lower arm for high frequencies in the experimental FRFs in Figure 2(b), also indicate there is a flexibility effect.

3. Improvement of the multibody pantograph model

Based on the analysis in Section 2.2, in this section, the pantograph model is improved to better match the experimental data, to give a reference model to use for optimisation of the lower suspension system in the following section. Firstly, parameter values of the head suspension are identified using the experimental FRF data. Then a non-ideal joint is introduced, using a rotational spring and damper in parallel at joint B. An additional DOFs are also added to approximately model the flexibility of the arms.

3.1. Identification of the head suspension parameters

Using the experimental FRFs, the head suspension parameters are identified in this sub-section. A sub-system of the pantograph in Figure 1, consisting of the pantograph head, suspension k_2, c_2, and the top of the stability arm is presented in Figure 4.

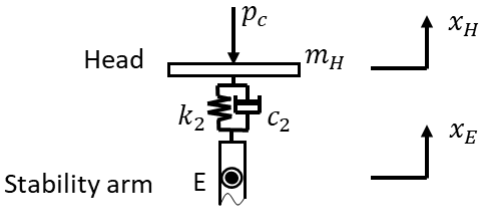

Figure 4. The simplified model of the head suspension system.

The equation of motion of the head is

$$m_H\ddot{x}_H(t) + \big(\dot{x}_H(t) - \dot{x}_E(t)\big)c_2 + \big(x_H(t) - x_E(t)\big)k_2 + p_c(t) = 0 \qquad (2)$$

where m_H is the mass of the head, $x_H(t)$ and $x_E(t)$ are the time history of displacements of the head and the top of the upper arm, respectively. Eq. (2) can be transferred to the Fourier domain as

$$\frac{m_H X_H(s)s^2}{P_c(s)} + \left(\frac{X_H(s)s}{P_c(s)} - \frac{X_E(s)s}{P_c(s)}\right)c_2 + \left(\frac{X_H(s)}{P_c(s)} - \frac{X_E(s)}{P_c(s)}\right)k_2 + 1 = 0 \qquad (3)$$

where $X_H(s)$, $X_E(s)$ and $P_c(s)$ are the displacements of the head and the top of the upper arm and the contact force in the Fourier domain and $s = 2\pi f\mathrm{j}$, $\mathrm{j} = \sqrt{-1}$. According to the definition of the FRF, $\mathrm{FRF_H}$ and $\mathrm{FRF_E}$ can be rewritten as complex numbers as

$$\mathrm{FRF_H}(f) = \frac{X_H(s)s^2}{P_c(s)} = a_H(f) + b_H(f)\mathrm{j} \tag{4}$$

$$\mathrm{FRF_E}(f) = \frac{X_E(s)s^2}{P_c(s)} = a_E(f) + b_E(f)\mathrm{j} \tag{5}$$

where $a_H = A_H\cos(\theta_H), b_H = A_H\sin(\theta_H), a_E = A_E\cos(\theta_E), b_E = A_E\sin(\theta_E)$. The amplitudes, *i.e.*, A_H, A_E, and phases, *i.e.*, θ_H, θ_E, of the experimental FRFs of the head and top of the upper arm are plotted in Figure 2, respectively. Substituting Eq. (4) and Eq. (5) into Eq. (3), we can get

$$m_H(a_H + b_H\mathrm{j}) + \left(\frac{b_H - a_H\mathrm{j}}{2\pi f} - \frac{b_E - a_E\mathrm{j}}{2\pi f}\right)c_2 + \left(-\frac{a_H + b_H\mathrm{j}}{(2\pi f)^2} + \frac{a_E + b_E\mathrm{j}}{(2\pi f)^2}\right)k_2 + 1 = 0. \tag{6}$$

Splitting Eq. (6) into its real and imaginary parts gives

$$\begin{cases} \mathrm{real}(c_2, k_2) = m_H a_H + \frac{b_H - b_E}{2\pi f}c_2 + \frac{-a_H + a_E}{(2\pi f)^2}k_2 + 1 = 0 \\ \mathrm{img}(c_2, k_2) = m_H b_H + \frac{-a_H + a_E}{2\pi f}c_2 + \frac{-b_H + b_E}{(2\pi f)^2}k_2 = 0 \end{cases}. \tag{7}$$

Assuming m_H is known accurately, the values of c_2 and k_2 for each individual frequency at which the FRFs are defined, can be obtained by solving Eq. (7). The results are shown in Figure 5. It is observed that the values of both c_2 and k_2 oscillate dramatically between 0Hz and 4Hz. This is because the displacement excitation had the same amplitude of 1 mm (see sub-section 2.1) for all frequency values, which leads to the contact force being too small at low frequencies compared with the noise in the measurement data. To avoid the effect of the noise, the experimental data for frequencies from 4Hz to 20Hz, over which the values of c_2 and k_2 are quite stable, are applied to find the constant values of c_2 and k_2 that minimise the square error function

$$g_1(c_2, k_2) = \sum_f \left(\left(\mathrm{real}(c_2, k_2)\right)^2 + \left(\mathrm{img}(c_2, k_2)\right)^2\right), f \in [4\mathrm{Hz}, 20\mathrm{Hz}]. \tag{8}$$

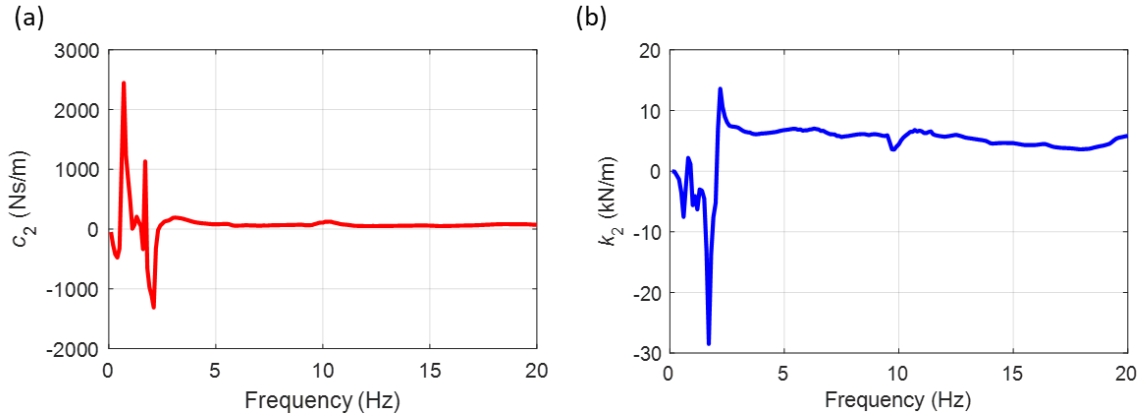

Figure 5. Values of c_2 and k_2 for each individual frequency from the experimental data by solving Eq. (7).

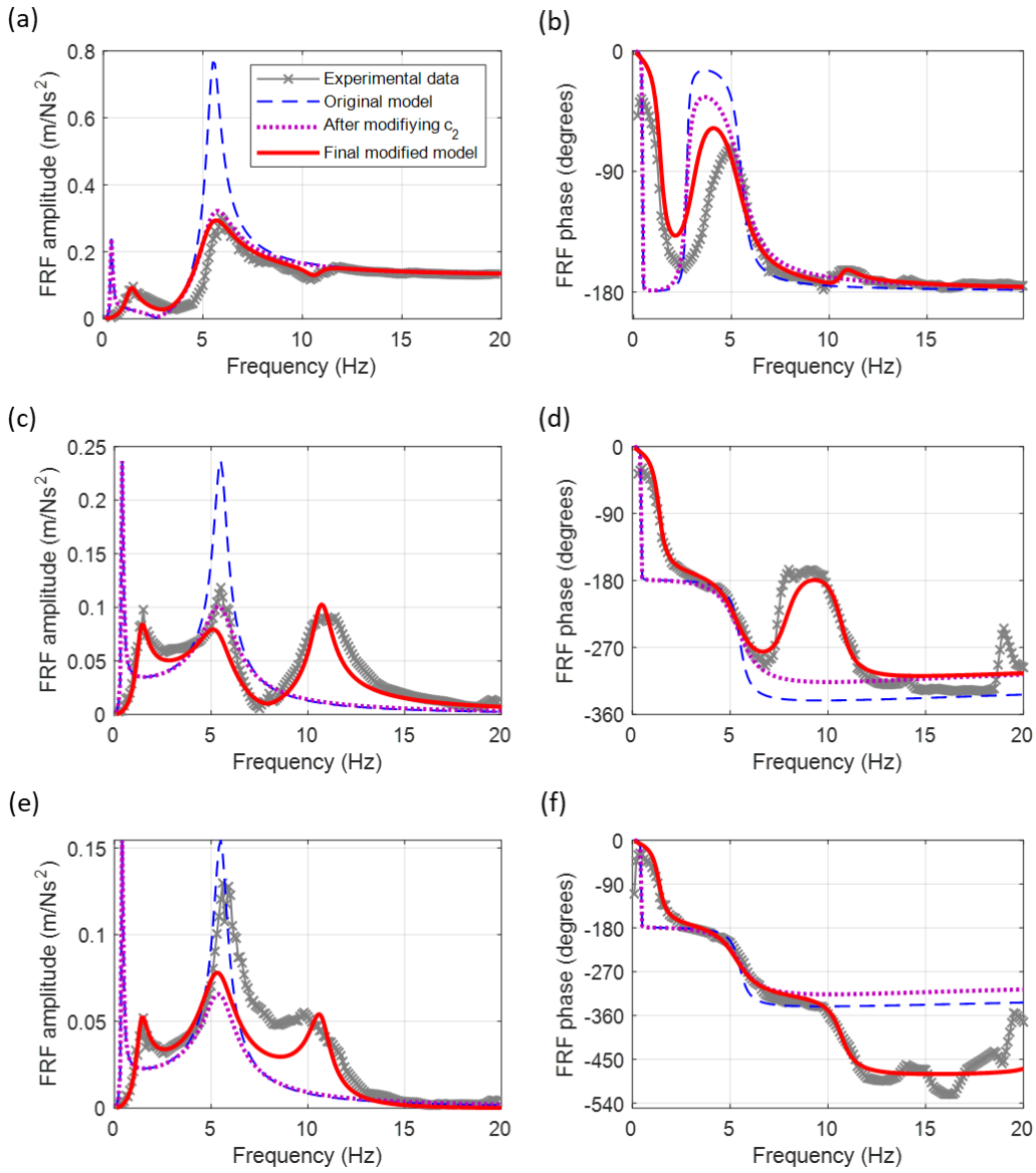

Figure 6. FRF amplitudes and phases of the (a)(b) head, (c)(d) top of the upper arm and (e)(f) top of the lower arm.

The MATLAB™ command *patternsearch* (Generalized pattern search method [48]) is applied to minimise $g_1(c_2, k_2)$ using the original values $c_{2\_original} = 26$ Ns/m and $k_{2\_original} = 7.20$ kN/m [45] as initial estimates. The values that minimise $g_1(c_2, k_2)$ are $c_2 = 65$ Ns/m and $k_2 = 7.20$ kN/m. It is noted that the identified value of c_2 is 2.5 times the default damping value while k_2 is the same as the default one, which is consistent with the analysis in sub-section 2.2. After modifying c_2, the FRFs of the numerical pantograph model are shown as pink dashed lines in Figure 6. The amplitudes of the second peaks for the head and the upper arm, in Figure 6(a)&(c), now match with the experimental data curves. The amplitude for the lower arm, in Figure 6(e), is now a little lower than that observed experimentally, but it is considered less important for the pantograph-catenary interaction than the amplitude for the head, where the contact takes place. The discrepancies between the model and experimental FRFs for the first and third peaks and in the phases are now addressed in the following sub-section.

3.2. Identification of the non-ideal joint and flexibility effect

In sub-section 2.2, the discussion of the mode analysis indicated that the stiffness and damping of the pantograph frame mechanism were both underestimated and at least one additional DOF is needed in the numerical model, which could arise from a flexibility effect. Therefore, the effect of non-ideal mechanical joints and flexibility of the frame are considered here. The non-ideal mechanical joint effect is modelled using a rotational spring k_f and damper c_f in parallel at joint B, as shown in Figure 7. It should be noted that only a single spring and single damper need be introduced since the rotations of all the joints in the pantograph frame are coupled in a mechanism. To capture the higher frequency modes, additional DOFs are required, which are introduced by modelling flexibility of the arms. This is achieved by introducing a rotational spring in each arm, k_u and k_l, at point B and point A, respectively. The model parameters of rigid bodies resulting from breaking arms can be updated according to their geometrical properties. In a sensitivity analysis, it was found that the FRFs are insensitive to the lower arm bending stiffness k_l, so for simplicity, its value was set to infinity. Hence, only the bending stiffness of the upper arm k_u is considered in this work, as shown in Figure 7. Its value was initially estimated from the arm's physical properties. As shown in Appendix 2, assuming the upper arm is a circular-hollow steel beam with 65 mm outside diameter and wall thickness 4 mm, its estimated bending stiffness is $\widetilde{k_u} \approx 120$ kNm/rad. Considering the uncertainty in the physical properties of the upper arm, its bending stiffness k_u was optimised to fit the experimental data using $k_u = \alpha\widetilde{k_u}$ where α is a coefficient in the range $\alpha \in [0.9,1.1]$. The parameters k_f, c_f and α identified simultaneously to minimise the total square FRF error between the present model and the experimental data, using the cost function

$$g_2(k_f, c_f, \alpha) = \sum_i \left(\sum_f \left(\mathrm{abs}\left(\mathrm{FRF}_i(k_f, c_f, \alpha, f) - \mathrm{FRF}_{\mathrm{i}}^{\mathrm{E}}(f) \right) \right)^2 \right), \quad i \in \{\mathrm{P}, \mathrm{E}, \mathrm{B}\}, f \in (0\mathrm{Hz}, 20\mathrm{Hz}] \tag{9}$$

where $\mathrm{FRF}_i(k_f, c_f, \alpha, f)$ and $\mathrm{FRF}_{\mathrm{i}}^{\mathrm{E}}(f)$ are the FRFs of the measurement points $i \in \{\mathrm{P}, \mathrm{E}, \mathrm{B}\}$ for the present model and the experimental data, respectively, and abs(·) is the modulus function. The results for the best fit are k_f= 6.46 kNm/rad, c_f= 334 Nms/rad and $\alpha = 1.03$, *i.e.*, $k_u = 124$ kNm/rad. Including these modifications to the model for the non-ideal joint effect and flexibility effect results in the FRFs shown as red-solid lines in Figure 6. The first peaks' amplitude and frequency match with the experimental data curves and the third peaks, around 11 Hz, are captured, as well as the amplitudes of the second peaks remaining similar to what they were after modifying c_2 only. For the phases, the low frequency of the red-solid lines in Figure 6(b), (d)&(f) match accurately with the experimental data. Furthermore, the phase gap between the top of the upper arm and top of the lower arm in high frequency has also been captured. It is worth to mention that the discrepancies of the first peaks and the third peaks are modified by the identification of the non-ideal joint effect and the flexibility effect, respectively. After all these calibration and validation, the proposed multibody model can describe accurately the dynamic response with clear physical meaning. This modified multibody pantograph can now be used as a default model to study the damping system design.

4. Inertance-integrated damping system design

In this section, a simplified pantograph-catenary model with time-varying parameters is developed here. The performance measure and the optimization process for the pantograph damping system are discussed in detail. An optimal inertance-integrated damping configuration is identified to improve the dynamic performance of the pantograph, with promising benefits in reduction of the standard deviation of the contact force observed. Lastly, relevant analyses

are carried out to understand the achieved benefits.

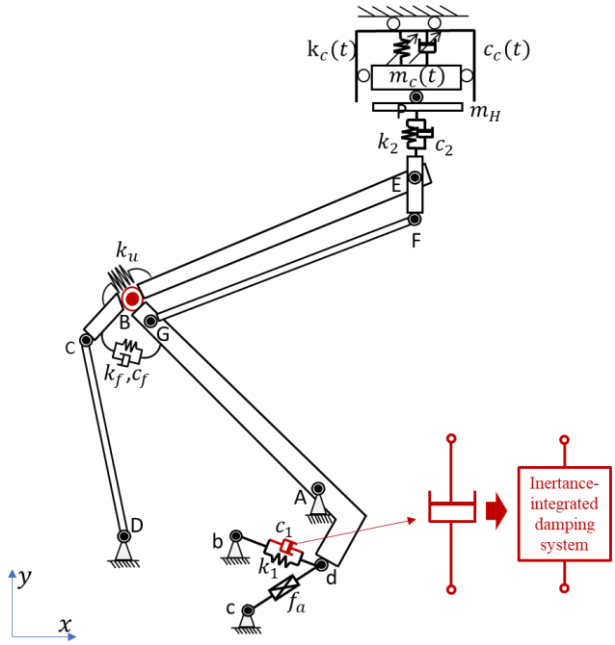

Figure 7. Modified multibody pantograph-catenary model and the modification to the base suspension.

4.1. Pantograph-catenary interaction model

The catenary systems are periodic structures generally composed of a messenger wire, contact wire, droppers and masts. The contact wire is the cable which carries the electricity and contacts with the pantograph head to supply the electric current to the railway vehicle. To establish an accurate mathematical model of the whole catenary system is awkward due to its distributed characteristics. Many FEM models of catenary systems have been established [8, 49-52], but these models are usually complex and they are not the focus of this paper.

In this paper, the focus is the design of a novel damping system for the high-speed train pantograph using the inertance-integrated damping technique. It is also noted that the pattern search methodology which is applied in the following optimization process requires a large number of iterations and therefore the dynamic models need to be reasonably fast and simple. A simplified catenary model which can represent the basic dynamic properties of the catenary system is sufficiently accurate for this purpose at this first concept design stage. Although the obtained responses using the simplified catenary model do not exactly match the realistic ones, this simplified catenary model favours the aim of the article which is not to evaluate the pantograph-catenary in realistic situations but to explore possible benefits in the use of inerters in a pantograph system. In a preliminary study, a lumped mass pantograph model coupled with a time-varying lumped mass catenary model was adopted to design an inertance-integrated damping system of the pantograph and significant dynamic performance benefit was observed [53]. For the sake of modelling simplification and calculation efficiency, the time-varying lumped mass catenary model in [6], as used in [53], is used in this work. As catenary systems are spatial-periodic structures, the equivalent parameters of the catenary system are spatial-periodic functions of the displacement x along the contact wire from a reference mast. If the operational speed is denoted as v_{op}, the distance $x = v_{op}t$. Hence, the equivalent parameters

of the catenary system can be converted to time-periodic functions and expressed as a Fourier series including the first three harmonics as

$$\begin{cases} m_c(t) = m_{c0} + \sum_{i=1}^{3} m_{ci} \cos\left(2\pi i \frac{v_{op}}{L} t\right) \\ c_c(t) = c_{c0} + \sum_{i=1}^{3} c_{ci} \cos\left(2\pi i \frac{v_{op}}{L} t\right) \\ k_c(t) = k_{c0} + \sum_{i=1}^{3} k_{ci} \cos\left(2\pi i \frac{v_{op}}{L} t\right) \end{cases} \tag{10}$$

where $\frac{v_{op}}{L}$ can be denoted as f_p called the pumping frequency [54], presenting the fundamental frequency of the pantograph passing a span with speed v_{op}. The equivalent mechanical parameters of the catenary system *i.e.*, the equivalent mass, stiffness and damper, denoted as m_c, k_c and c_c, respectively, present periodic behaviour along each span with the harmonics of the first three integer multiples of the pumping frequency. The parameters of the catenary model, *i.e.*, m_{ci}, c_{ci} and k_{ci}, are detailed in [6]. Pantograph-catenary interaction is depicted in Figure 7. The state variables of the pantograph and the catenary system are combined by coupling their dynamical equations. The contact wire is an additional lumped mass body coupled with the pantograph model. Hence, a revolute joint between the contact points of the catenary and the head is adopted to model the contact between them in this paper, see Figure 7. The contact force is evaluated as the vertical reaction force of this revolute joint applied on the head. In this way, as contact loss is not explicitly modelled, each output of the model has been checked to ensure that the contact force does not become positive and hence that this modelling approach for the contact is valid.

4.2. Performance measure and optimization procedure

In this work, the structure-based approach [44] is used to design a beneficial inertance-integrated pantograph damping system. The network layouts representing the topology of the mechanical components are firstly proposed. Then, the parameter values of each element in the mechanical network are selected using an optimization method. The total candidate layout sets **S** are shown in Figure 8 where the inerter, damper and spring are labelled as *b*, *c* and *k*, respectively. $S_{default}$ in Figure 8 is the conventional damper in the existing design of the pantograph. Four simple candidate layouts are proposed here to assess the potential benefits of employing an inertance-integrated damping system in the pantograph. A one-element layout, S_0, with a single inerter, two two-element layouts, S_1 and S_2, with one inerter and one damper, in parallel and in series, respectively, and a three-element layout, S_3, known as the TID system [55] with one inerter, one damper and one spring, are considered in this work.

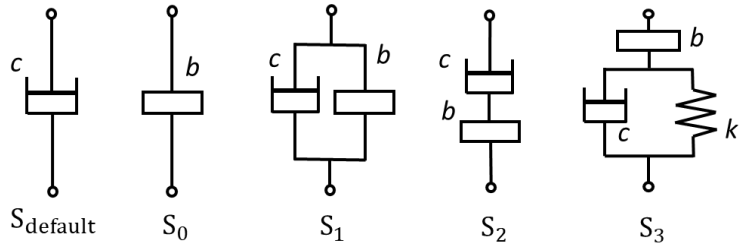

Figure 8. Candidate layout set **S**.

In practice, in order to ensure the efficiency of power transmission between the contact wire and the pantograph head, an optimal mean contact force F_m is suggested in EN 50367:2012 [56]. Meanwhile, the standard deviation of the contact force σ is required to be smaller than $0.3F_m$ to ensure the probability that the contact force is lower than $0.1F_m$ is less than 0.27%,

assuming a Gaussian distribution [56]. These specifications aim to ensure the percentage of time for electric arcing – the main reason for electrical wear of the contact wire and the head – is smaller than 0.2%. Hence, in this work, the standard deviation of the contact force σ is used as the assessment performance.

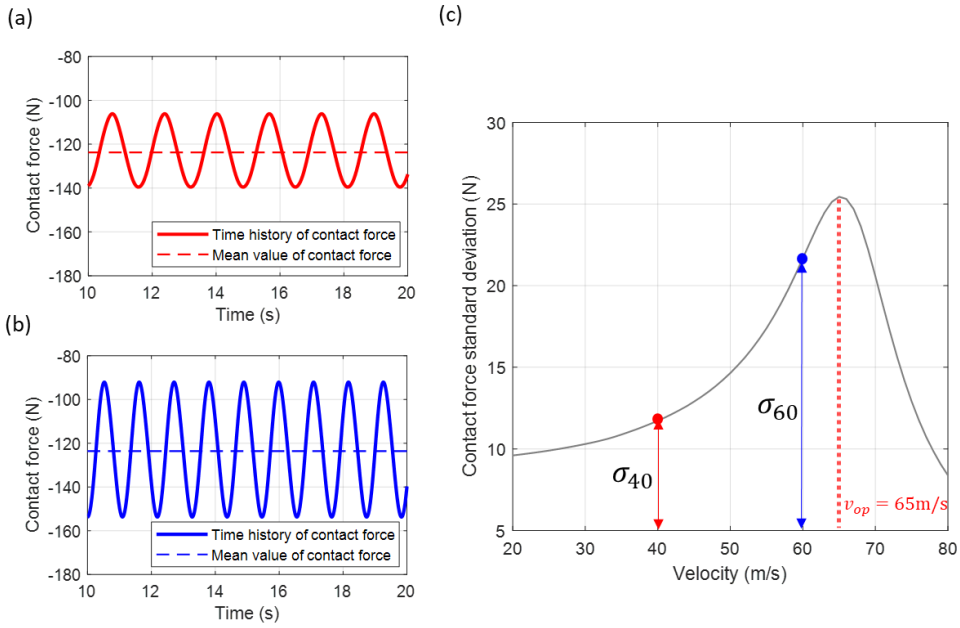

Figure 9. Contact force for (a) 40 m/s and (b) 60 m/s, (c) contact force standard deviations across the whole range of operational speeds from 20 m/s to 80 m/s.

The proposal is to reduce the standard deviation of the pantograph-catenary contact force through designing the base suspension system using inertance-integrated damping, as shown in Figure 7. The standard deviation of the contact force σ for each individual vehicle speed can be evaluated via the corresponding contact force time history. For example, for the default damping system with a conventional damper, the contact force time histories for 40 m/s and 60 m/s are shown in Figure 9(a) and (b), respectively. Considering operational speeds between 20 m/s and 80 m/s, the standard deviation of the contact force for the default damping system is shown in Figure 9(c), where the values for 40 m/s and 60 m/s are marked with red and blue points, respectively. It is noted that in Figure 9(c) the default pantograph-catenary system has a maximum value of the standard deviation $\sigma_{\max} = 25.45$ N at an operational speed $v_{op} = 65$ m/s. Note that given the level of fidelity of the catenary model employed, it is challenging to make the simulated responses satisfy an industrial standard for a real system, such as EN 50367, over the full operating range. Simulations of the system considered do satisfy EN 50367 near the operational speed of 65 m/s, which is the main speed we are interested in. In this work, the optimization aim is to minimise $\sigma_{\max}$ over the whole operational speed range. The cost function $J(\boldsymbol{\varphi}_i)$ of the optimization is identified as

$$J(\boldsymbol{\varphi}_i) = \sigma_{\max}(\boldsymbol{\varphi}_i), i \in \mathbf{S}, v \in [20\ \text{m/s}, 80\ \text{m/s}] \quad (11)$$

where $\boldsymbol{\varphi}_i$ is the design variables for candidate layout i. For all the optimizations carried out in the damping system design, the MATLAB™ command *patternsearch* (Generalized pattern search method [48]) is used. A number of sets of random initial values are used to find the optimum parameter values to minimise the cost function J.

4.3. Results for optimised inertance-integrated damping systems

The optimization results, based on the verified multibody pantograph model from Section 3, are given in Table 1. It can be observed that the mean contact forces of the proposed inertance-integrated damping configurations are kept almost constant, closely matching that of the default damper. In order to make a fair comparison, the default layout (a conventional damper) is firstly optimised for our cost function. The optimised default layout $S_{default\_opt}$ results in a 0.04% reduction in σ_{max} compared with $S_{default}$, indicating that the contact force standard deviation cannot be reduced significantly using the default damper. In contrast, all the proposed inertance-integrated configurations, *i.e.*, S_0, S_1, S_2 and S_3, achieve a significant 40.67% reduction in σ_{max}. For S_0, the optimum inertance value is 10745 kg. Note that the value of this inertance does not correspond to the mass of the device achieving this inertance. With a fluid-based inerter [57, 58], the ratio of the resultant inertance b to the actual fluid mass m is $\left(\frac{D_1}{D_2}\right)^4$ where D_1 and D_2 are the piston's and tube's effective diameters, respectively. A significantly large inertance can be achieved with much smaller fluid mass via designing these two diameters. For example, if $\frac{D_1}{D_2} = 10$, the optimized inertance 10745 kg can be obtained with the actual fluid mass as 1.07 kg. Hence, the inertance value obtained in this paper is totally practical for pantograph suspensions. The result of S_1 implies that the inerter dominates the performance improvement while the damper in parallel contributes little. Hence, S_1 can be simplified to S_0, that is, the damper in parallel can be ignored. This can be concluded from the fact that the optimised value of the damper in parallel is so small and the inerter value is very close to the optimum inerter value of S_0. For S_2, the value of the damper in series reaches 2.7×10^{10} Ns/m, which implies that the damper in series tends to a rigid connection, again suggesting that the inerter dominants the performance improvement in S_2. It has been checked that setting the damper value of S_2 to be infinite, that is, replacing the damper in S_2 to a rigid connection, there is no significant reduction in performance of S_2. Hence, S_2 can also be simplified to S_0 without any significant reduction in performance. For S_3, the value of the damper and spring reaches 1.5×10^{11} Ns/m and 2.5×10^{11} N/m and a similar argument can also be applied to S_3. Therefore, the fact that S_1, S_2 and S_3 can all be converted to S_0 gives weight to the argument that the single inerter configuration S_0 is the optimum design among the proposed candidate configurations in this case.

Table 1 Optimization results

Layout	Configuration parameters			σ_{max} (N)	Reduction (%)	Velocity for σ_{max} (m/s)	Mean contact force (N)
	b (kg)	*c* (Ns/m)	*k* (N/m)				
$S_{default}$	\	600	\	25.45	\	65.0	121.5
$S_{default\_opt}$	\	2563	\	25.44	0.04%	65.0	121.5
S_0	10745	\	\	15.10	40.67%	63.0	121.1
S_1	10728	5	\	15.10	40.67%	63.0	121.1
S_2	10703	$\rightarrow \infty$	\	15.10	40.67%	63.0	121.9
S_3	10703	$\rightarrow \infty$	$\rightarrow \infty$	15.10	40.67%	63.0	121.9
S_1^*	10733	600	\	15.23	40.16%	63.0	121.1

The relationship between the contact force standard deviation and inertance for different parallel dampers at 65 m/s is as shown visually in Figure 10. It indicates that about 10000 kg of inertance can minimise the standard deviation of the contact force while the smaller or larger inertance can deteriorate the contact performance. It is also observed that any inertance value

between 0 and the optimum value can be beneficial to reduce the contact force standard deviation correspondingly. It also noticed that the presence of a damper in parallel with inerter has a negative effect on reducing the contact force standard deviation, a further indication why S_1 should be simplified to S_0. This does not mean there is no natural damping in the system but shows that an additional damper at the base cannot help improve the contact performance. Considering that the original damper in parallel may have a function that is not included in our present cost function, for example, suppressing transient vibrations when raising or lowering the pantograph, the performance of an additional configuration, S_1^* is investigated. The layout of S_1^* is the same as S_1, but the parallel damper is fixed to 600 Ns/m, *i.e.*, the original value of conventional damper, and the inerter is then optimised. It turns out that S_1^*, see the blue line in Figure 10, can retain almost the same performance benefit as S_0, see the red line in Figure 10.

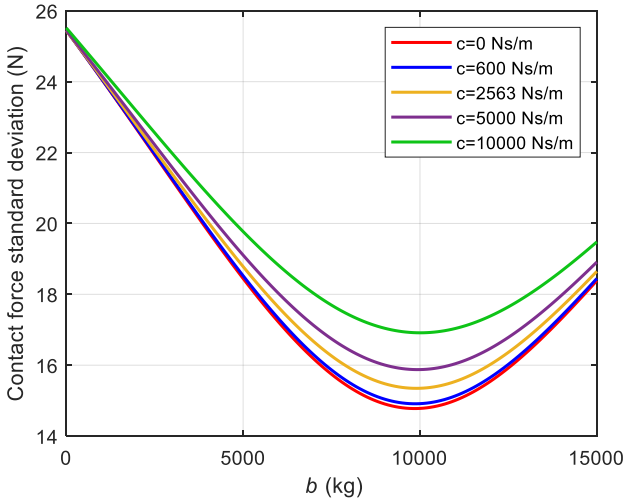

Figure 10. Standard deviations of the contact force against inertance for different parallel dampers at 65 m/s.

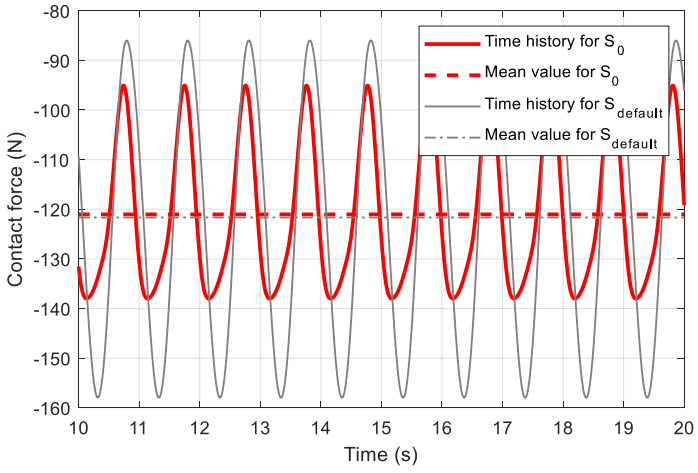

Figure 11. Time histories and mean values of the contact force for S_0 and $S_{default}$ based pantographs at $65 m/s$.

In order to investigate the performance improvement of S_0 in detail, analysis in the time domain is considered. Time histories of the contact force for S_0 and $S_{default}$ at 65 m/s are shown in Figure 11. It is clear that the amplitude of contact force variation is reduced significantly for

S_0 compared with $S_{default}$. Further, acceleration response for catenary alone with a constant upward contact force is evaluated. The constant upward contact force whose value is selected as the value of the mean contact force of the default pantograph-catenary system acts on catenary along with a sequence of operational speeds, *i.e.*, a sequence of pumping frequencies f_p. The corresponding acceleration magnitude U_c of the catenary against different pumping frequencies f_p is investigated as shown in Figure 12, indicating the natural frequency of the catenary system is 1 Hz. Note that the theoretical natural frequency of the catenary system can be approximated from Eq. (10) as $\frac{1}{2\pi}\sqrt{\frac{k_{c0}}{m_{c0}}} \approx 1$ Hz, coinciding with the resonance frequency in Figure 12. For the pantograph system alone, the FRFs for the head in the magnitude of $S_{default}$ and S_0 based pantographs are shown in Figure 13. Note that the FRF for the head of $S_{default}$ based pantograph in Figure 13 is the same as the FRF curve of the modified model in Figure 6(a). Compared with $S_{default}$, the first resonance frequency of the pantograph head for S_0 is shifted to 1 Hz from 1.5 Hz, see Figure 13, coinciding with the natural frequency of the catenary system. This results in the vibration of the pantograph head aligning with that of the catenary system which appears to reduce the contact force variation. This can also explain the discussion about Figure 10, that is, the fact that the inclusion of 10000 kg of inertance tunes the pantograph first resonance frequency coinciding with the natural frequency of the catenary regulates the fluctuation of the contact force.

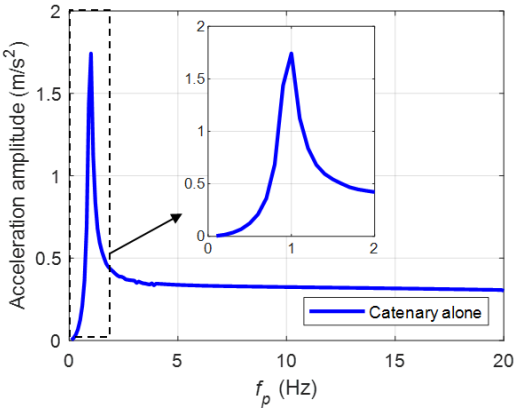

Figure 12. Acceleration amplitude for the catenary alone with a constant upward contact force against the pumping frequency.

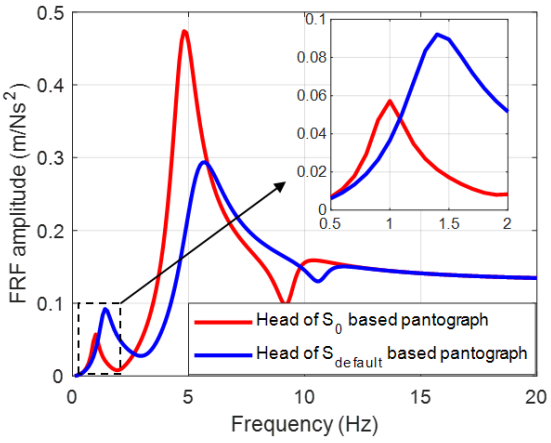

Figure 13. Comparison of amplitudes of FRF for head between $S_{default}$ and S_0 based pantographs.

Furthermore, the displacements of the catenary alone with the constant upward contact force and coupling with the $S_{default}$ and S_0 based pantographs are also evaluated in Figure 14. The catenary oscillation displacement amplitude across the whole operational speed range is shown in Figure 14(a) indicating the amplitudes of the catenary coupling with the pantographs are reduced compared with the catenary alone with the constant upward contact force. The displacement amplitude of the catenary coupling with S_0 based pantograph is also slightly reduced compared with the default pantograph indicating that, with the S_0 based pantograph, the cable motion is acceptable. Figure 14(b) shows the catenary displacements in the time domain at 65 m/s. It is clear that the displacement amplitudes of the catenary coupling with pantographs are smaller than the catenary alone with the constant upward contact force. Meanwhile, the phase gap of the catenary displacement between the catenary alone with the constant upward contact force and catenary coupling with the pantograph is reduced for S_0 compared with $S_{default}$. These means that with S_0, the pantograph head tends to have the same phase relative to the catenary system, so as the contact force between them is reduced.

The standard deviation of the contact force across the whole range of operational speed are presented in Figure 15 for the $S_{default}$ and S_0 based pantographs. There is a 40% reduction for the S_0 based pantograph compared with the default one and it remains lower than for the default one for all velocities less than 75 m/s.

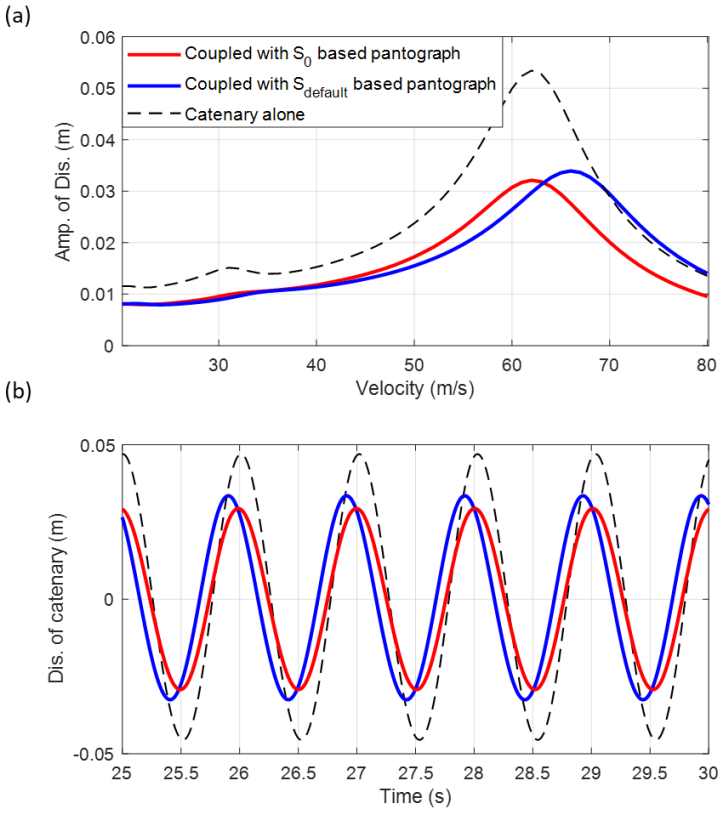

Figure 14. (a) Displacement amplitudes across the whole operational speed range. (b) displacement time histories of the catenary with the constant upward contact force and coupling with $S_{default}$ and S_0 based pantographs at 65 m/s.

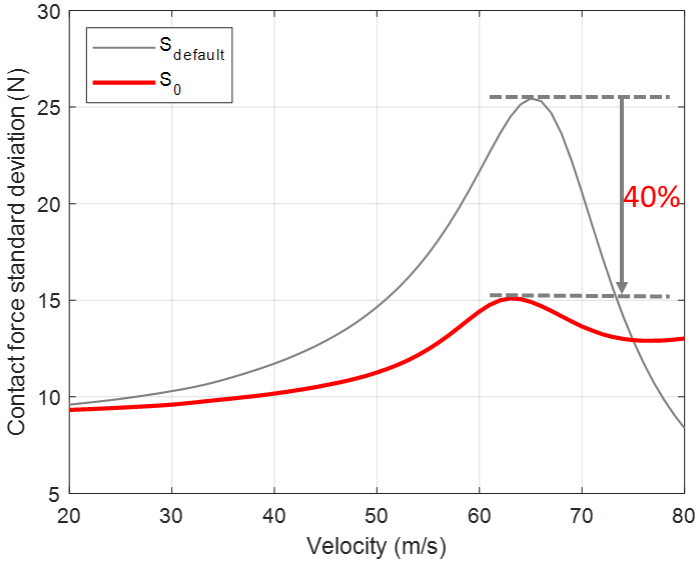

Figure 15. The standard deviation of the contact force for $S_{default}$ and S_0 based pantographs across the whole operational speed range.

5. Conclusions and future developments

In this paper, a multibody pantograph model with clear physical meaning is developed based on a previously published model. Some discrepancies are observed in terms of the FRFs compared with experimental data. Basic mode shapes of the pantograph are investigated using the experimental FRF data, which indicates characteristics of the internal reaction between each physical component of the pantograph and reveals the sources of the observed discrepancies. To better match the experimental data, the head suspension damping is updated and additional model details are introduced in the model to allow for non-ideal joints and flexibility of the pantograph upper arm. A methodology to identify the pantograph parameters with practical physical meaning, using optimization methods, is proposed. After the calibration, the modified model can match the experimental data accurately and is used as the default model for the design of an improved damping system. The structure-based inertance-integrated damping method is applied and optimised configurations are obtained for the pantograph damping system. The results suggest that a 40 % reduction in the maximum standard deviation of the contact forces over the whole range of train speeds is possible to achieve using inerter, based on this specified pantograph-catenary modelling approach considered. It might be possible that these more in-depth and detailed studies realize a lesser actual reduction on standard deviation. However, as it is the main aim of the article, the results obtained suggest that the proposed concept is worth being further researched and developed. The inerter with the corresponding optimum values can be realised using a ball-screw [30] or fluid-based inerter [57, 58]. Given the space limit in the pantograph system, the device size can be altered by changing the screw pitch of the ball-screw inerter, or adjusting the ratio of the piston's effective diameter to the tube's diameter of the fluid-based inerter. Subsequently, the inerter can be designed and manufactured, and then replace the conventional damper in the pantograph system. Analyses of the contact force in the time domain for the pantograph with the inerter are carried out, which shows that the amplitude of the contact force of the S_0 based pantograph reduced significantly compared with the default one. Furthermore, mode analysis of the pantograph and the catenary shows that in optimizing the inertance-integrated damping system the first resonant frequency of the pantograph is tuned to the natural frequency of the catenary and that this appears to

regulate the pantograph-catenary contact force oscillation. In this paper, the numerical implementation of the inertance-integrated damping system suggests promising results in improving pantograph-catenary contact performance. Building on the results obtained in this study, future developments are worthwhile using other pantograph types and more detailed catenary models, which will allow further assessment, including singularities such as overlaps and gradients, of the inertance-integrated damping technology in such conditions.

Acknowledgements

Ming Zhu is supported by the China Scholarship Council-University of Bristol joint PhD Scholarships Programme. Sara Ying Zhang is supported by a National Natural Science Foundation of China under Grant No.52008259. Jason Zheng Jiang is supported by an EPSRC Fellowship (EP/T016485/1). Jo*ã*o Pombo and Pedro Antunes are supported by FCT, through IDMEC, under LAETA, project UIDB/50022/2020.

References

[1] SNCF (PARIS). European optimised pantograph catenary interface. 2008. (Project no. 012440). Retrieved from https://trimis.ec.europa.eu/project/european-optimised-pantograph-catenary-interface#tab-docs.
[2] Bobillot A, Massat JP, Mentel JP. Design of pantograph-catenary systems by simulation. In: 9th World Congress on Railway Research (WCRR); 22 May 2011, Lille, France.
[3] Poetsch G, Evans J, Meisinger R, et al. Pantograph/catenary dynamics and control. Veh Syst Dyn. 1997; 28(2-3): 159-195.
[4] Ambrósio J, Pombo J, Pereira M, et al. Recent developments in pantograph-catenary interaction modelling and analysis. Int J Railw Technol. 2012; 1(1): 249-278.
[5] Wu TX, Brennan MJ. Basic analytical study of pantograph-catenary system dynamics. Veh Syst Dyn. 1998;30(6): 443-456.
[6] Pisano A, Usai E. Contact force regulation in wire-actuated pantographs via variable structure control and frequency-domain techniques. Int J Control. 2008; 81(11): 1747-1762.
[7] Facchinetti A, Bruni S. Hardware-in-the-loop hybrid simulation of pantograph–catenary interaction. J Sound Vib. 2012; 331(12): 2783-2797.
[8] Ambrósio J, Pombo J, Antunes P, et al. PantoCat statement of method. Veh Syst Dyn. 2015; 53(3): 314-328.
[9] Ambrósio J, Pombo J, Pereira M, et al. A computational procedure for the dynamic analysis of the catenary-pantograph interaction in high-speed trains. J Theor Appl Mech. 2012; 50(3): 681-699.
[10] Ambrósio J, Pombo J, Pereira M. Optimization of high-speed railway pantographs for improving pantograph-catenary contact. Theor Appl Mech Lett. 2013; 3(1): 013006.
[11] Ambrósio J, Rauter F, Pombo J, et al. A flexible multibody pantograph model for the analysis of the catenary–pantograph contact. In: Multibody Dyn. Dordrecht: Springer. 2011: 1-27.
[12] Ambrósio J, Pombo J, Rauter F, et al. A memory based communication in the co-simulation of multibody and finite element codes for pantograph-catenary interaction simulation. In: Multibody Dyn. Dordrecht: Springer. 2009: 231-252.
[13] Antunes P, Magalhães H, Ambrosio J, et al. A co-simulation approach to the wheel–rail contact with flexible railway track. Multibody Syst Dyn. 2019; 45(2): 245-272.
[14] Collina A, Fossati F, Papi M, et al. Impact of overhead line irregularity on current collection and diagnostics based on the measurement of pantograph dynamics. Proc Inst Mech Eng Part F J Rail Rapid Transit. 2007; 221(4): 547-559.

[15] Nåvik P, Rønnquist A, Stichel S. Variation in predicting pantograph–catenary interaction contact forces, numerical simulations and field measurements. Veh Sys Dyn. 2017; 55(9): 1265-1282.
[16] Song Y, Antunes P, Pombo J, et al. A methodology to study high-speed pantograph-catenary interaction with realistic contact wire irregularities. Mech Mach Theory. 2020: 103940.
[17] Pombo J, Ambrósio J, Pereira M, et al. Influence of the aerodynamic forces on the pantograph–catenary system for high-speed trains. Veh Syst Dyn, 2009; 47(11): 1327-1347.
[18] Carnevale M, Facchinetti A, Maggiori L, et al. Computational fluid dynamics as a means of assessing the influence of aerodynamic forces on the mean contact force acting on a pantograph. Proc Inst Mech Eng Part F J Rail Rapid Transit. 2016; 230(7): 1698-1713.
[19] Song Y, Liu Z, Wang H, et al. Nonlinear analysis of wind-induced vibration of high-speed railway catenary and its influence on pantograph–catenary interaction. Veh Syst Dyn. 2016; 54(6): 723-747.
[20] Shing AWC, Wong PPL. Wear of pantograph collector strips. Proc Inst Mech Eng Part F J Rail Rapid Transit. 2008, 222(2): 169-176.
[21] Wang H, Núñez A, Liu Z, et al. Analysis of the evolvement of contact wire wear irregularity in railway catenary based on historical data. Veh Syst Dyn. 2018; 56(8): 1207-1232.
[22] Pombo J, Ambrósio J. Multiple pantograph interaction with catenaries in high-speed trains. J Comput Nonlinear Dyn. 2012; 7(4).
[23] Pombo J, Antunes P. A comparative study between two pantographs in multiple pantograph high-speed operations. Int J Railw Technol. 2013; 2(1): 83-108.
[24] Carnicero A, Jimenez-Octavio JR, Sanchez-Rebollo C, et al. Influence of track irregularities in the catenary-pantograph dynamic interaction. J Comput Nonlinear Dyn. 2012; 7(4).
[25] Pombo J, Ambrósio J. Environmental and track perturbations on multiple pantograph interaction with catenaries in high-speed trains. Comput Struct. 2013; 124: 88-101.
[26] Antunes P, Ambrósio J, Pombo J, et al. A new methodology to study the pantograph–catenary dynamics in curved railway tracks. Veh Syst Dyn. 2019.
[27] Park TJ, Han CS, Jang JH. Dynamic sensitivity analysis for the pantograph of a high-speed rail vehicle. J Sound Vib. 2003; 266(2): 235-260.
[28] Kim JW, Chae HC, Park BS, et al. State sensitivity analysis of the pantograph system for a high-speed rail vehicle considering span length and static uplift force. J Sound Vib. 2007; 303(3-5): 405-427.
[29] Zhou N, Zhang W. Investigation on dynamic performance and parameter optimization design of pantograph and catenary system. Finite Elem Anal Des. 2011; 47(3): 288-295.
[30] Smith MC. Synthesis of mechanical networks: the inerter. IEEE Trans Autom Control. 2002; 47(10): 1648-1662.
[31] Firestone FA. A new analogy between mechanical and electrical systems. J Acoust Soc Am. 1933; 4(3): 249-267.
[32] Evangelou S, Limebeer DJN, Sharp RS, et al. Steering compensation for high-performance motorcycles. In: 43rd IEEE Conference on Decision and Control (CDC); 2004 Dec 14-17; Nassau, Bahamas. IEEE; 2004.
[33] Smith MC, Wang FC. Performance benefits in passive vehicle suspensions employing inerters. Veh Syst Dyn. 2004; 42(4): 235-257.
[34] Zhang SY, Zhu M, Li Y, et al. Ride comfort enhancement for passenger vehicles using the structure-immittance approach. Veh Syst Dyn. 2019: 1-22.
[35] Wang FC, Liao MK, Liao BH, et al. The performance improvements of train suspension systems with mechanical networks employing inerters. Veh Syst Dyn. 2009; 47(7): 805-830.

[36] Jiang JZ, Matamoros-Sanchez AZ, Goodall RM, et al. Passive suspensions incorporating inerters for railway vehicles. Veh Syst Dyn. 2012; 50(sup1): 263-276.
[37] Lewis TD, Li Y, Tucker GJ, et al. Improving the track friendliness of a four-axle railway vehicle using an inertance-integrated lateral primary suspension. Veh Syst Dyn. 2019; 1-20.
[38] Wang FC, Hong MF, Chen CW. Building suspensions with inerters. P I Mech Eng C-J Mech. 2010; 224(8): 1605-1616.
[39] Lazar IF, Neild SA, Wagg DJ. Using an inerter-based device for structural vibration suppression. Earthq Eng Struct Dyn. 2014; 43(8): 1129-1147.
[40] Zhang SY, Jiang JZ, Neild S. Optimal configurations for a linear vibration suppression device in a multi-storey building. Struct Control Health. 2017; 24(3): e1887.
[41] Li Y, Jiang JZ, Neild S. Inerter-based configurations for main-landing-gear shimmy suppression. J Aircraft. 2016; 54(2): 684-693.
[42] Li YY, Zhang SY, Jiang JZ, et al. Passive vibration control of offshore wind turbines using the structure immittance approach. In: Proceedings of the International Conference on Noise and Vibration Engineering; 17-19 Sep 2018, Leuven.
[43] Luo J, Macdonald JHG, Jiang JZ. Identification of optimum cable vibration absorbers using fixed-sized-inerter layouts. Mech Mach Theory. 2019; 140: 292-304.
[44] Zhang SY, Jiang JZ, Neild SA. Passive vibration control: a structure–immittance approach. P Roy Soc A-Math Phy. 2017, 473(2201): 20170011.
[45] Vieira R. High Speed Train Pantograph Models Identification, Master's thesis, Instituto Superior Tecnico, University of Lisbon, Lisbon, Portugal, 2016.
[46] Resta F, Facchinetti A, Collina A, et al. On the use of a hardware in the loop set-up for pantograph dynamics evaluation. Veh Syst Dyn. 2008; 46(S1): 1039-1052.
[47] Ambrósio J, Pombo J. A unified formulation for mechanical joints with and without clearances/bushings and/or stops in the framework of multibody systems. Multibody Syst Dyn. 2018; 42(3): 317-345.
[48] Audet C, Dennis JJE. Analysis of generalized pattern searches. SIAM J Optimiz. 2002, 13(3): 889-903.
[49] Song Y, Liu Z, Wang H, et al. Nonlinear modelling of high-speed catenary based on analytical expressions of cable and truss elements. Veh Sys Dyn. 2015; 53(10): 1455-1479.
[50] Collina A, Bruni S. Numerical simulation of pantograph-overhead equipment interaction. Veh Syst Dyn. 2002; 38(4): 261-291.
[51] Cho YH. Numerical simulation of the dynamic responses of railway overhead contact lines to a moving pantograph, considering a nonlinear dropper. J Sound Vib. 2008; 315(3): 433-454.
[52] Lee JH, Park TW, Oh HK, et al. Analysis of dynamic interaction between catenary and pantograph with experimental verification and performance evaluation in new high-speed line. Veh Syst Dyn. 2015, 53(8): 1117-1134.
[53] Zhu M, Zhang SY, Jiang JZ, et al. Enhancing the dynamic performance of a pantograph-catenary system via inerter-based damping technology. International Conference on Noise and Vibration Engineering; 17-19 Sep 2018; Leuven.
[54] Wereley NM. Analysis and control of linear periodically time varying systems [dissertation]. Cambridge (MA): Massachusetts Institute of Technology; 1990.
[55] Lazar IF, Neild SA, Wagg DJ. Using an inerter-based device for structural vibration suppression. Earthq Eng Struct Dyn, 2014; 43(8): 1129-1147.
[56] European Committee for Electrotechnical Standardization. Railway applications. Current collection systems. Technical criteria for the interaction between pantograph and overhead line (to achieve free access). Brussels: CENELEC; 2012. Standard No. EN 50367:2012+A1:2016.
[57] Swift SJ, Smith MC, Glover AR, et al. Design and modelling of a fluid inerter. Int. J. Control. 2013, 86(11): 2035-2051.

[58] Liu X, Jiang JZ, Titurus B, et al. Model identification methodology for fluid-based inerters. Mech Syst and Signal Process. 2018, 106: 479-494.
[59] Shabana AA. Computational dynamics. New York (NY): Wiley; 2009.
[60] Nikravesh PE. Computer-aided analysis of mechanical systems. Upper Saddle River (NJ): Prentice-Hall, Inc.; 1988.
[61] Baumgarte J. Stabilization of constraints and integrals of motion in dynamical systems. Comput Method Appl Mech Eng. 1972; 1(1): 1-16.
[62] Flores P, Machado M, Seabra E, et al. A parametric study on the Baumgarte stabilization method for forward dynamics of constrained multibody systems. J Comput Nonlinear Dyn. 2011, 6(1).
[63] Gear C. Simultaneous numerical solution of differential-algebraic equations. IEEE Trans Circuit Theory, 1971, 18(1): 89-95.

Appendix 1 Equations of motion of the multibody model

A typical multibody model is an assemblage of rigid bodies constrained by kinematic mechanical joints and acted upon by external forces [59]. The general forces applied to the system components may be the result of mechanical elements, for example, springs, dampers, actuators, or externally applied forces, such as contact forces or gravity. The configuration of the multibody system can be described by *n* Cartesian coordinates **q**, and a set of *m* algebraic kinematic independent holonomic constraints **Φ**, written in a compact form as

$$\boldsymbol{\Phi}(\mathbf{q}, t) = \mathbf{0} \tag{A1}$$

Differentiating, and doubling differentiating Eq. (A1) with respect to time yields the velocity and acceleration constraint equations

$$\boldsymbol{\Phi}_{\mathbf{q}}\dot{\mathbf{q}} + \boldsymbol{\Phi}_t = \mathbf{0} \tag{A2}$$

$$\boldsymbol{\Phi}_{\mathbf{q}}\ddot{\mathbf{q}} = -\boldsymbol{\Phi}_{tt} - \left(\boldsymbol{\Phi}_{\mathbf{q}}\dot{\mathbf{q}}\right)_{\mathbf{q}}\dot{\mathbf{q}} - 2\boldsymbol{\Phi}_{\mathbf{q}t}\dot{\mathbf{q}} = \boldsymbol{\gamma} \tag{A3}$$

where $(\cdot)_{\mathbf{q}} = \frac{\partial(\cdot)}{\partial \mathbf{q}}$, $(\cdot)_{\mathbf{q}t} = \frac{\partial^2(\cdot)}{\partial \mathbf{q}\partial t}$, $(\cdot)_t = \frac{\partial(\cdot)}{\partial t}$, $(\cdot)_{tt} = \frac{\partial^2(\cdot)}{\partial t^2}$ and $\dot{(\cdot)} = \frac{d(\cdot)}{dt}$, $\ddot{(\cdot)} = \frac{d^2(\cdot)}{dt^2}$, respectively. The equations of motion of a constrained rigid multibody system can be expressed as [60]

$$\mathbf{M}\ddot{\mathbf{q}} = \mathbf{g}_{\mathrm{e}} + \mathbf{g}_{\mathrm{c}} \tag{A4}$$

where **M** is the generalized mass matrix, $\mathbf{g}_{\mathrm{e}}$ is the generalized external force vector, which contains all external forces and moments, and $\mathbf{g}_{\mathrm{c}}$is the generalized constraint forces vector, which contains the reaction forces and moments resulting from the constraints. $\mathbf{g}_{\mathrm{c}}$ can be expressed in terms of the Jacobian matrix of the constraints and the vector of Lagrange multipliers

$$\mathbf{g}_{\mathrm{c}} = -\boldsymbol{\Phi}_{\mathrm{q}}^{\mathrm{T}}\boldsymbol{\lambda} \tag{A5}$$

where $\boldsymbol{\lambda}$ is the vector that contains *m* unknown Lagrange multipliers associated with *m* holonomic constraints. Substituting Eq. (A5) into Eq. (A4) yields

$$\mathbf{M}\ddot{\mathbf{q}} + \boldsymbol{\Phi}_{\mathrm{q}}^{\mathrm{T}}\boldsymbol{\lambda} = \mathbf{g}_{\mathrm{e}} \tag{A6}$$

In the dynamic analysis, a unique solution is obtained when the constraint equations are considered simultaneously with the equations of motion with the appropriate initial conditions. Therefore, Eq. (A3) is appended to Eq. (A6), yielding a system of differential-algebraic equations that are solved for $\ddot{\boldsymbol{q}}$ and $\boldsymbol{\lambda}$. This system is given by

$$\begin{bmatrix} \mathbf{M} & \mathbf{\Phi}_\mathbf{q}^{\mathrm{T}} \\ \mathbf{\Phi}_\mathbf{q} & \mathbf{0} \end{bmatrix} \begin{bmatrix} \ddot{\mathbf{q}} \\ \boldsymbol{\lambda} \end{bmatrix} = \begin{bmatrix} \mathbf{g}_\mathrm{e} \\ \boldsymbol{\gamma} \end{bmatrix} \tag{A7}$$

The set of differential-algebraic equations of motion, Eq. (A7), does not explicitly ensure that the position and velocity kinematic constraint equations, *i.e.*, Eq. (A1) and (A2), are satisfied. Consequently, in the case of long-time simulations, the original constraint equations are quickly violated due to the integration process. Therefore, in order to keep the potential constraint violation under control, the Baumgarte constraint stabilization method [61] is applied in our work. Recall that using Eq. (A3), the second time derivative of the constraint equations can be written as

$$\ddot{\mathbf{\Phi}} = \mathbf{\Phi}_\mathbf{q}\ddot{\mathbf{q}} - \boldsymbol{\gamma} = \mathbf{0}. \tag{A8}$$

In Baumgarte's constraint stabilization method, the second time derivative of the constraint equations is modified and is written in the following form

$$\ddot{\mathbf{\Phi}} + 2\alpha\dot{\mathbf{\Phi}} + \beta^2\mathbf{\Phi} = \mathbf{0} \tag{A9}$$

where $\dot{\mathbf{\Phi}} = \mathbf{\Phi}_\mathbf{q}\dot{\mathbf{q}} + \mathbf{\Phi}_t$, $\alpha > 0$, $\beta \neq 0$. Eq. (A9) is a differential equation for a closed-loop system in terms of the kinematic constraint equations, where the terms $2\alpha\dot{\mathbf{\Phi}}$ and $\beta^2\mathbf{\Phi}$ play the role of control terms by feeding back the position and velocity of constraint violations. Substituting Eq. (A8) into Eq. (A9) leads to

$$\mathbf{\Phi}_\mathbf{q}\ddot{\mathbf{q}} = \boldsymbol{\gamma} - 2\alpha\dot{\mathbf{\Phi}} - \beta^2\mathbf{\Phi} \tag{A10}$$

Using Eq. (A10), the equations of motion of the multibody system can be modified and written as

$$\begin{bmatrix} \mathbf{M} & \mathbf{\Phi}_\mathbf{q}^{\mathrm{T}} \\ \mathbf{\Phi}_\mathbf{q} & \mathbf{0} \end{bmatrix} \begin{bmatrix} \ddot{\mathbf{q}} \\ \boldsymbol{\lambda} \end{bmatrix} = \begin{bmatrix} \mathbf{g}_\mathrm{e} \\ \boldsymbol{\gamma} - 2\alpha\dot{\mathbf{\Phi}} - \beta^2\mathbf{\Phi} \end{bmatrix} \tag{A11}$$

In this work, the values $\alpha = \beta = 5$ are chosen following the parameter selection process outlined in reference [62]. The integration process is performed using a variable step and variable order integration algorithm, ode15s solver (Gear's method [63]) in MATLAB$^{\mathrm{TM}}$.

Appendix 2. Process of estimating $\widetilde{k_u}$

The main span of the upper arm, BE (Figure 1), can be modelled as a flexible cantilever beam fixed at point B with a transverse load P applied at E. The deflection of the end E is then $\delta = Pl^3/3EI$ where $l \approx 2$ m is the length BE, $E \approx 200 \times 10^9$ Pa is Young's modulus and I is the second moment of area of the beam. In this work, the second moment of area for the hollow circular section can be calculated as

$$I = \frac{\pi}{64}(D^4 - (D - 2d)^4) \approx 4 \times 10^{-7}\ \mathrm{m}^4 \tag{A12}$$

where D is the outside diameter, d is the thickness.

The cantilever beam can be simplified as a rigid beam constrained by a revolute joint and an equivalent rotational spring $\widetilde{k_u}$ at B. An angle θ of the rigid beam can be generated when the load P is applied at the other end. Using a small angle approximation, $\theta \approx \frac{\delta}{l}$. The moment at point B is $M_\mathrm{B} = Pl$. The equivalent rotational stiffness at point B can be evaluated as

$$\widetilde{k_u} = \frac{M_\mathrm{B}}{\theta} \approx \frac{Pl^2}{\delta} = \frac{3EI}{l} = 120\ \mathrm{kN/rad}. \tag{A13}$$